

# Pion contamination in the Muon Ionisation Cooling Experiment (MICE) muon beam

**M. Bogomilov**

*Department of Atomic Physics, St. Kliment Ohridski University of Sofia, Sofia, Bulgaria*

**M. Bonesini**

*Sezione INFN Milano Bicocca, Dipartimento di Fisica G. Occhialini, Milano, Italy*

**D. Orestano, L. Tortora**

*Sezione INFN Roma Tre e Dipartimento di Matematica e Fisica, Università di Roma Tre, Roma, Italy*

**O.M. Hansen**

*CERN, Geneva, Switzerland*

*Also at University of Oslo, Norway*

**Y. Karadzhov**

*Department of Atomic Physics, St. Kliment Ohridski University of Sofia, Sofia, Bulgaria*

*DPNC, Section de Physique, Université de Genève, Geneva, Switzerland*

**R. Bayes, J.C. Nugent, F.J.P. Soler**

*School of Physics and Astronomy, Kelvin Building, The University of Glasgow, Glasgow, UK*

The international Muon Ionisation Experiment (MICE) will perform a systematic investigation of ionisation cooling of a 200 MeV/c muon beam at the Rutherford Appleton Laboratory ISIS facility. It is essential to limit the contamination of pions in the MICE muon beam to be below 1% in order to perform a precise measurement of ionisation cooling of muons. The MICE muon beam has been commissioned and it was demonstrated in a previous paper that this beam meets the emittance and muon momentum requirements to perform the MICE physics programme. In this note we also show that the MICE beam meets the stringent pion contamination requirements, using particle identification detectors that are used to characterise the MICE beam, showing good agreement with the expectation. It is shown that the upper level for the pion contamination was found to be  $f_{\pi} < 0.69\%$  at 90% C.L., assuming statistical errors only and  $f_{\pi} < 1.0\%$  at 90% C.L., including statistical and systematic errors. A similar procedure applied to the G4Beamline and MAUS Monte Carlo simulation yields a pion contamination of  $f_{\pi} < 0.86\%$  at 90% C.L., assuming statistical errors only and  $f_{\pi} < 1.7\%$  at 90% C.L., including statistical and systematic errors. This agrees with the Monte Carlo expectation of  $(0.22 \pm 0.01)\%$ . These data demonstrate that the muon beam designed and built at the ISIS facility meets all the requirements to carry out a comprehensive physics programme that aims to measure ionisation cooling using the MICE cooling channel.

# 1 Introduction

The international Muon Ionisation Cooling Experiment (MICE) [1], at the Rutherford Appleton Laboratory (RAL), will demonstrate the principle of ionisation cooling as a technique for reduction of the phase-space volume occupied by a muon beam. Ionisation cooling channels are required for neutrino factories [2–6] and muon colliders [7–9], as this is the only known technique that can achieve the required cooling performance within the short muon lifetime.

Ionisation cooling [10] is accomplished by passing the muon beam through a low- $Z$  material (the “absorber”), in which it loses energy via ionisation, reducing both the longitudinal and transverse components of momentum. The lost energy is restored by accelerating the beam such that the longitudinal component of momentum is increased, while the transverse components remain unchanged. The net effect is to reduce the emittance of the beam, hence the volume of transverse phase space that it occupies. Beam transport through the absorbers and accelerating structures is achieved using a solenoid focusing lattice. While a modest transverse cooling factor ( $\sim 3.4$ ) is required in the current neutrino factory design [6], much greater ( $\sim 10^6$ ) six dimensional (6D) cooling in all phase space components is required for a muon collider.

# 2 MICE Apparatus

A schematic diagram of the MICE cooling channel is shown in Figure 1. It follows the design principles of a single lattice cell of the cooling channel for the International Design Study for a Neutrino Factory [6], and has evolved from the original cooling channel design in [11]. It consists of one primary lithium hydride (LiH) absorber, two secondary absorbers, two Focus Coils and two 201 MHz RF cavities that provide longitudinal acceleration of  $\sim 10.3$  MV/m. The two superconducting Focus Coils are used for the optics of the cooling channel by ensuring that the transverse beta function is minimised at the position of the absorbers, thereby increasing the cooling performance of the channel.

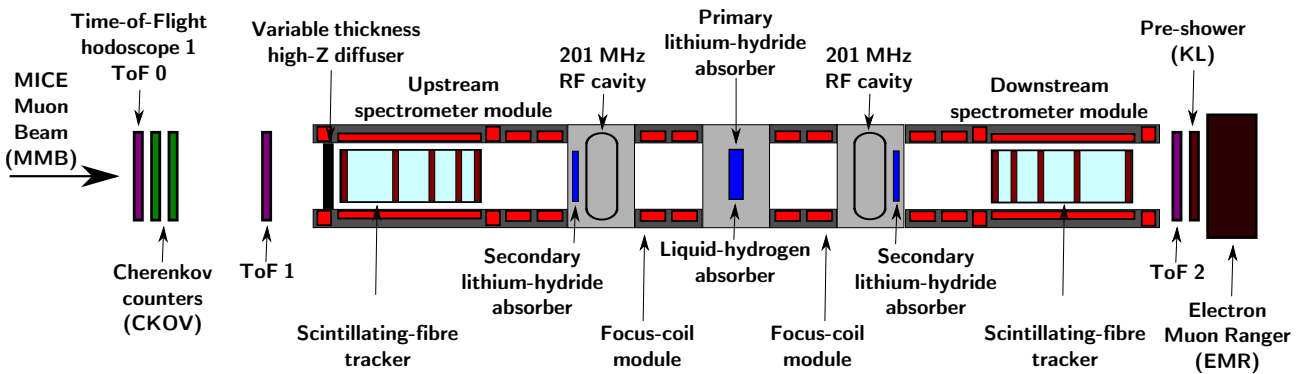


Figure 1: Schematic view of the MICE cooling channel, with three LiH absorbers (one primary absorber in the centre and two secondary absorbers), two RF cavities and two Focus Coil solenoid magnets that define the MICE optics, sandwiched between two identical trackers, inside superconducting solenoids.

A reduction in normalised emittance of 6% is expected for a muon beam entering the cell with a nominal momentum of  $200 \text{ MeV}/c$  and normalised emittance  $\epsilon_N = 5.8\pi \text{ mm} \cdot \text{rad}$ . The tracking spectrometers [12] upstream and downstream of the cooling cell consist of scintillating fibre tracking modules inside solenoid magnetic fields, to measure the emittance before and after the cooling cell. These are required to measure the normalised emittance,  $\epsilon_N$  with an absolute precision of  $\sigma_{\epsilon_N}/\epsilon_N = 0.1\%$ . Conventional emittance measurement techniques based on beam-profile monitors cannot achieve the required precision, so MICE has been designed

as a single-particle experiment, in which each muon is measured using state-of-the-art particle detectors and the bunched muon-beam is reconstructed offline [13].

The instrumentation upstream of the MICE cooling cell includes a particle identification (PID) system that allows a pure muon beam to be selected. The PID system consists of scintillator time-of-flight  $x/y$  hodoscopes TOF0 and TOF1 [14] read at both edges by fast conventional Hamamatsu R4998 photomultipliers [15], and two threshold Cherenkov counters Ckova and Ckovb [16]. The TOF system is required to reject electrons and pions in the incoming muon beam with an efficiency in excess of 99%. Furthermore, the precision of the TOF time measurement must be sufficient to allow the phase at which the muon enters the RF cavities to be determined to  $5^\circ$ . To satisfy these requirements, the resolution of each TOF station must be  $\sim 50$  ps. The TOF resolutions obtained were 55 ps for TOF0, 53 ps for TOF1 and 50 ps for TOF2 [17, 18].

The two Cherenkov detectors have been designed to guarantee muon-identification purities better than 99.7% in the momentum range  $210 \text{ MeV}/c$  to  $365 \text{ MeV}/c$  [19]. The TOF and the Cherenkov systems work in combination with the upstream tracking spectrometer [12], which will measure the momentum of the incoming particles [20] in MICE Step IV [21], to extract the particle identification.

Downstream of the cooling channel, a final scintillator time-of-flight  $x/y$  hodoscope (TOF2 [22]) and a calorimeter system allow muon decays to be identified and rejected. The calorimeter system for MICE consists of the KLOE-Light (KL) lead-scintillator sampling calorimeter, similar to the KLOE design [23], but with thinner lead foils, designed to serve as a preshower for the Electron Muon Ranger (EMR) totally active scintillating detector. The main roles of the KL and EMR detectors are to distinguish muons from decay electrons, and to provide a distinction between muon and pion signals. In this paper, however, the pion contamination of the MICE muon beam was measured on a statistical basis before the MICE tracking spectrometers and the EMR were installed. The analysis was accomplished by combining the TOF velocity information with the KL calorimetric information. KL is a lead-scintillator sampling calorimeter, composed of scintillating fibres and extruded lead foils, with active volume of  $93 \times 4 \times 93 \text{ cm}^3$ . It has 21 cells and the light from its scintillating fibres is collected by 42 Hamamatsu R1355 PMTs. The PMT signals are sent via a shaper module to 14 bit CAEN V1724 flash ADCs. The shapers stretch the signal in time in order to match the flash ADC sampling rate. A detailed description of KL is given in [20].

### 3 MICE Muon Beam

The required transverse emittance range of the MICE muon beam is  $3 \leq \epsilon_N \leq 10 \pi \text{ mm} \cdot \text{rad}$ , with mean momenta  $140 \leq p_\mu \leq 240 \text{ MeV}/c$  and root-mean-squared (RMS) momentum widths of  $\sim 20 \text{ MeV}/c$ . A pneumatically operated “diffuser”, consisting of tungsten and brass irises of variable thickness, is placed at the entrance to the upstream spectrometer solenoid in order to generate the required range of emittance in the beam. In order to perform the muon emittance measurement with the required accuracy of 0.1%, it is essential to limit the intrinsic pion and electron contamination of the muon beam to less than 1%. The particle identification system is designed to identify electrons and pions in the cooling channel at a level so that any remnant contamination is such that the muon emittance measurement can be performed with the required accuracy.

The design of the MICE muon beam is briefly summarised here (see Figure 2) and is reported in [20]. Pions produced by the momentary insertion of a titanium target [24] into the 800 MeV ISIS proton beam are captured using a quadrupole triplet (Q1–3) and are transported to a first dipole magnet (D1), which selects particles of a desired momentum bite into the decay solenoid (DS). Muons produced by pions decaying in the DS are momentum-selected using a second dipole magnet (D2) and are focussed onto the diffuser by a quadrupole channel (Q4–6 and Q7–9). By capturing pions of transverse momentum up to  $\sim 70 \text{ MeV}/c$ , and increasing their path length by deflecting them onto helical trajectories, the decay solenoid increases the probability of muon capture between D1 and D2 by an order of magnitude compared to a simple quadrupole channel. In

115 positive-beam running, a borated polyethylene absorber of variable thickness is inserted into the beam just downstream of DS in order to suppress the high rate of protons that can be produced at the target [25].

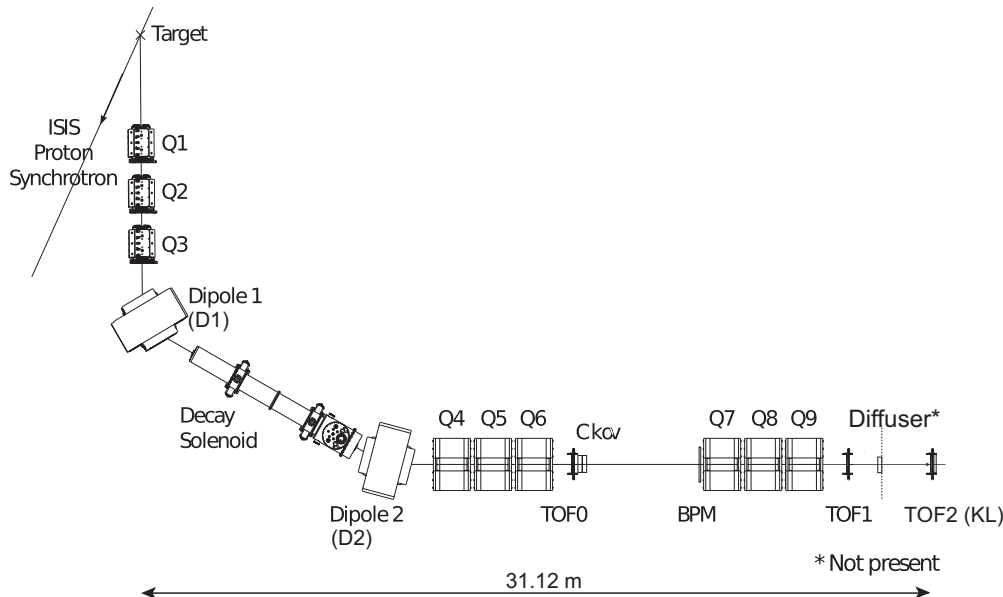


Figure 2: Top view of the MICE beam line with its instrumentation, as used in Step I. The distances between TOF0 (TOF1) and TOF1 (TOF2) are respectively 773.3 cm and 198.8 cm.

The composition and momentum spectra of the beams delivered to MICE are determined by the interplay between the two bending magnets D1 and D2. In normal (“ $\pi \rightarrow \mu$  mode,” or “muon”) operation, D2 is set to half the momentum of D1, selecting backward-going muons in the pion rest frame and producing an almost pure muon beam. Pions of high momentum that do not decay may be present in the beam and it is this small contamination that is the purpose of the measurement in this paper. In the absence of a precise momentum measurement from the spectrometer, single-particle pion identification, by combining with the velocity information from either the TOF or Cherenkov measurements, is not possible. Therefore, the measurement will be performed on a statistical basis using the KL and TOF information. Alternatively, by setting  $p_{D1} \simeq p_{D2}$ , a mixed beam containing pions, muons and electrons is obtained. This “calibration mode” is used to calibrate the particle identification detectors and will be used in the analysis to provide “templates” for the particle identification performance of the KL and TOF detectors.

The nominal values of the beam momenta  $p_\mu$  are defined as those evaluated at the centre of the central LiH absorber in the final cooling demonstration configuration, taking into account the energy loss by the particles along the muon beam, which include the TOF and Cherenkov detectors, the proton absorber (for positive polarity beams), the diffuser and the air along the particle trajectories. For example, a momentum at D2 of  $p_{D2} = 238 \text{ MeV}/c$  implies a momentum value of  $p_\mu = 200 \text{ MeV}/c$  at the centre of the LiH absorber.

MICE Step I data were taken in December 2011 with the configuration shown in Figure 2, including the upstream TOF0 and TOF1 detectors, Cherenkov detectors and the downstream TOF2 and KL detectors, which were operated in a temporary position about 2 m downstream of TOF1. The correspondence between beam momenta at various points in the MICE beam for the muon beam configuration and the different calibration beams used in this analysis is summarised in Table 1.

Table 1: Summary of runs used in this analysis. The muon runs correspond to a nominal setting  $(\varepsilon_N, p_\mu) = 6\pi$  mm·rad , 200 MeV/c. Reported momenta are at the entrance of the quoted detectors.

Muon runs				
$p_{D2}$ (MeV/c)	$p_{TOF0}$ (MeV/c)	$p_{TOF1}$ (MeV/c)	$p_{TOF2}$ (MeV/c)	# events ( $10^3$ )
238	220	204	190	270
Calibration runs				
$p_{D2}$ (MeV/c)	$p_{TOF0}$ (MeV/c)	$p_{TOF1}$ (MeV/c)	$p_{TOF2}$ (MeV/c)	# events ( $10^3$ )
222	217	194	181	195
258	254	231	219	235
280	276	254	242	167
294	290	268	257	354
320	316	295	284	265
362	358	337	326	448

## 4 Contamination in the MICE muon beam

### 4.1 Monte Carlo simulations

140 The pion contamination under the muon peak was estimated using the G4beamline simulation package [26] and the MICE Applications User Software (MAUS) package [27] to simulate detector response. The position of all the beam line and detector elements in the beam is given in Table 2.

Figure 3 (left) compares distributions of flight time from TOF0 to TOF1, obtained in typical beam configurations, for reconstructed positive-beam data and corresponding to Monte Carlo simulations of  $6\pi$  mm · rad positive muon beams with nominal beam momentum  $p_\mu = 200$  MeV/c, compared to data. The Step I geometry has now been tuned so that the data and the Monte Carlo peaks now sit on top of each other. Figure 3 (right) shows the momentum distribution at TOF1 of the electron, pion and muon peaks for the same Monte Carlo simulation, showing that the pion contamination under the muon peak is predominantly due to high momentum pions that are selected by the D2 dipole magnet and are subsequently transported by the beam. Since the pions that contaminate the muon sample have higher momenta than the muons, their time-of-flights are consistent. Since the muons and pions have equivalent velocities, the Cherenkov detector cannot be used to distinguish them, since there is no independent method to measure their momentum. Therefore, the residual pion contamination in the beam, after the selection of the muon component via time-of-flight, can only be measured from the spectrum of energy released in KL. The pion contamination is a function of the position where it is measured. According to the G4beamline simulation, the contamination under the muon peak at TOF0 is estimated to be 1.78%, reducing to 0.38% at TOF1 and 0.25% at the KL position. The contamination under the muon peak is summarised in Figure 4.

### 4.2 Pion contamination measurement with TOF and KL detectors

#### 4.2.1 TOF detector distributions

160 The residual pion contamination in the beam, after the selection of the muon component via time-of-flight, can be measured from the spectrum of energy released in KL. Due to the broad momentum acceptance of the MICE beam line in  $\pi \rightarrow \mu$  mode, the pions contaminating the muon sample have higher momenta than the muons, in order for the time-of-flight to be consistent. This prevents the use of Cherenkov detectors in MICE Step I to

Table 2: Position of the MICE beam line elements and detectors for the pion contamination runs during Step I data taking.

Element	Distance from target along beam axis (cm)
Q1	3000.0
Q2	4400.0
Q3	5800.0
D1	7979.1
Decay Solenoid	12210.7
Proton absorber	14880
GVA1	15050.0
D2	15808.1
Q4	17661.6
Q5	18821.6
Q6	19981.6
TOF0	21088.0
Ckova	21251.5
Ckovb	21910.9
Q7	25293.7
Q8	26453.7
Q9	27613.7
TOF1	28793.1
TOF2	31198.1
KL	31323.1

fully tag pions, in absence of a precise determination of momentum for beam particles (see Figure 3, right).

165 Figure 5 shows distributions of the time-of-flight of particles between TOF0 and TOF1, with a positive  $\pi \rightarrow \mu$  beam of a nominal momentum of 200 MeV/c (Figure 5-(a)) and with with a calibration beam with  $p_{D2} \simeq 222$  MeV/c (Figure 5-(b)). An electron peak is observable and well separated from the main muon peak for the  $\pi \rightarrow \mu$  beam, but the level of the pion contamination under the muon peak is difficult to assess, as the two TOF distributions overlap. However, for the calibration beam with  $p_{D2} \simeq 222$  MeV/c, the electron, muon and pion  
170 peaks are well separated by their time-of-flight.

The pion contamination is studied in positive muon beam runs with nominal beam momentum 200 MeV/c ( $p_{D2} = 238$  MeV/c) and with collected statistics of about  $270 \times 10^3$  triggers (Table 1). The study is performed as a function of the time-of-flight of the beam particles in three distinct time-of-flight intervals (referred to below as “Points 1-3”) whose choice is dictated by the availability of calibration data for which the specified  
175 interval is populated mainly by muons or mainly by pions. Pairs of calibration runs for which muons and pions present time-of-flight values within the same range (see Table 3) are defined for each point and are used to benchmark the KL response to muons or to pions of given time-of-flight. Figure 5-(a) shows the three points highlighted in grey in the time-of-flight distribution of particles in the MICE muon beam.

The widths of the intervals were determined by taking into account the overlap regions between the calibration runs. In each of these time-of-flight intervals the spectra of the KL response can be extracted for muons and pions separately from the calibration runs. These spectra are then used as templates for the response to muons and pions in that time-of-flight interval for the muon runs. As an example, Figure 6 shows the time-of-flight distributions in two paired beam settings. The interval between 28.0–28.6 ns in the TOF0–TOF1 time-of-flight (point 2) is populated mainly by muons for one beam setting and by pions for the other. These configurations  
185 were also modelled using the Monte Carlo simulations using the same TOF0–TOF1 time-of-flight intervals. For

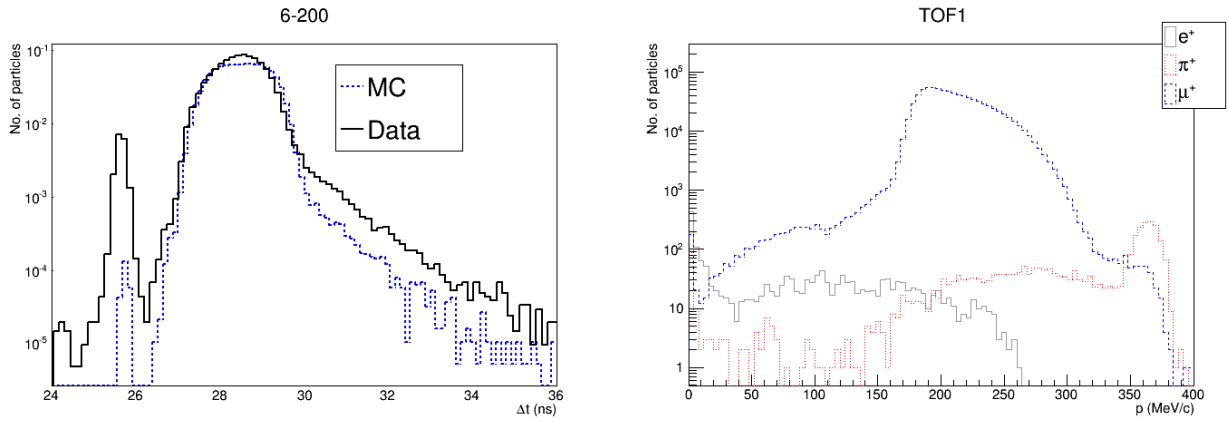


Figure 3: Left: Time-of-flight distributions between TOF0 and TOF1 for data and Monte Carlo simulation for a  $6\pi$  mm · rad positive muon beam with nominal beam momentum  $p_\mu = 200$  MeV/c. Right: Momentum distribution for beam particles at TOF1 for a simulated positive  $6\pi$  mm · rad at 200 MeV/c (a cut between 26.2 and 32 ns on the time-of-flight between TOF0 and TOF1 is applied).

Table 3: Paired beam settings for three time-of-flight intervals (also called Points).

	TOF interval, ns	muons from runs with $P_{D2}$ (MeV/c)	pions from runs with $P_{D2}$ (MeV/c)
Point 1	27.4 – 27.9	294	362
Point 2	28.0 – 28.6	258	320
Point 3	28.9 – 29.6	222	280

example, the 27.4–27.9 ns interval (point 1) pair of beams is shown in Figure 7 and the 28.0–28.6 ns interval (point 2) is shown in Figure 8

#### 4.2.2 KL detector distributions

In the range 200–300 MeV/c, the minimum ionising responses of muons and pions in the KL are similar, but pions can also undergo hadronic interactions, which are visible as a tail in the KL response to pions. The KL response to a particle is defined in terms of the product of the digitised signals from the left and right sides of each scintillator slab divided by their sum:

$$ADC_{\text{product}} = 2 \frac{ADC_{\text{left}} \times ADC_{\text{right}}}{ADC_{\text{left}} + ADC_{\text{right}}},$$

where the factor of 2 is present for normalisation. The ADC product is carried out to compensate for light attenuation in the scintillator. It can be shown that the normalised ADC product of the PMT signals is less sensitive to the particle hit position along the fibre length if the properties of the optical fibre are characterised by two attenuation lengths, with one much shorter than the other [28, 29].

The normalised ADC products are summed for all scintillator slabs in the KL that have a signal above a threshold. The KL response to muons and pions in calibration runs and to an unknown particle mix in the  $\pi \rightarrow \mu$  beam mode are added together for the three TOF intervals (Points 1, 2 and 3) and shown in Figure 9. An additional constraint was required that only one track was present in both the time-of-flight detectors, associated to only one hit in the KL detector. The distribution for the pions displays a larger tail than the muon

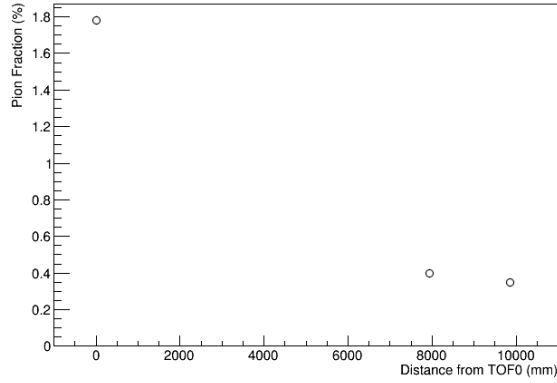


Figure 4: Pion contamination in a  $6\pi$  mm · rad positive muon beam, at momentum  $p_\mu = 200$  MeV/c at different positions along the beam line as deduced from G4beamline and MAUS Monte Carlo simulations. The three points refer to the position of the TOF0, TOF1, and KL positions in the MICE Step I configuration. The  $z$  coordinate is in mm in the MICE reference system, with the origin moved to the position of TOF0. The simulation includes a proton absorber of 83 mm. A cut between 26.2 and 32 ns on the time-of-flight between TOF0 and TOF1 is applied.

one, due to the presence of hadronic interactions. This feature is used in the following analysis to estimate on a statistical basis the MICE muon beam contamination.

The MAUS simulation used to depict the KL response was fine-tuned to take into account the features of the normalised ADC product in the Monte Carlo, to be compared to the data. The following features were taken into account:

- Poisson smearing of the photons produced in the scintillation fibres and the photoelectrons produced at the photocathode of the PMT;
- the photomultiplier gain, assumed to be Gaussian with the mean equal to the photomultiplier gain ( $\sim 2 \times 10^6$ ) and the standard deviation equal to half of the gain [30];
- the conversion factors from photoelectrons to ADC (250,000 PE/ADC), from MeV to photoelectrons (0.000125 MeV/PE), the two-component scintillating fibre attenuation lengths (2400 mm and 200 mm), the scintillating fibre collection efficiency (3.6%), the light-guide collection efficiency (85%) and the photomultiplier tube quantum efficiency (26%), in order to obtain  $\sim 1060$  ADC counts for a minimum ionising peak.

The Monte Carlo simulation of the KL response to muons and pions for the calibration runs and for the simulated  $\pi \rightarrow \mu$  beam are compared to data in Figure 10. The result of the fit of the Monte Carlo pion and muon templates to the simulated  $\pi \rightarrow \mu$  beam is also shown in Figure 10 (bottom-right). Finally, the comparison of the Monte Carlo simulations of the two templates, the  $\pi \rightarrow \mu$  beam and the fitted result are shown in Figure 11. The features of the simulated Monte Carlo KL response to pions and muons follows closely that from the data in Figure 9.

## 5 Fits to the pion contamination in the muon beam

The fraction of pions and muons in the  $\pi \rightarrow \mu$  beam is extracted by exploiting the information contained in the full KL response spectrum for the sums of the three time-of-flight intervals. The method employs the ROOT TFractionFitter method [31, 32] based upon fitting the normalised muon and pion templates to the actual KL



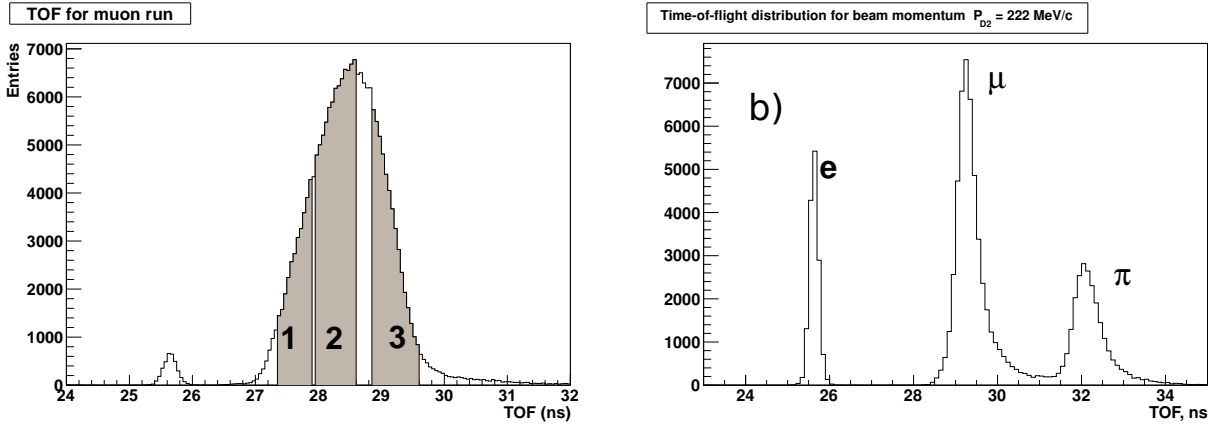


Figure 5: (a) Time of flight distributions between TOF0 and TOF1 for a positive muon beam with a nominal momentum of 200 MeV/c (the left peak is due to electrons). (b) Positive “calibration” beam taken with  $p_{D2} = 222$  MeV/c. The pion contamination is studied in three time-of-flight intervals, highlighted in grey.

spectrum in the MICE data. This was carried out for both the extracted MICE data and for the simulated Monte Carlo distributions for the  $6\pi$  mm·rad, 200 MeV/c  $\pi \rightarrow \mu$  beam. The fits for the sum of the three time-of-flight windows (27.4 ns – 27.9 ns, 28.0 ns – 28.6 ns, 28.9 ns – 29.6 ns) are shown as histograms for the data in Figure 9 and for the Monte Carlo simulation in Figure 11. The fits take into account both data and template statistical uncertainties, through a standard likelihood fit using Poisson statistics, allowing the templates to vary within the statistical errors.

The data from the  $6\pi$  mm·rad, 200 MeV/c muon beam encompassing the three time-of-flight windows includes  $N_b = 129870$  beam events. The fraction of muon and pion events were allowed to converge without any physical restrictions. The total fitted number of muon events was  $N_\mu = 130169$ , which yielded a negative number of pion events  $N_\pi = -303 \pm 509$ . Similarly, for the Monte Carlo simulation, the fitted number of muon events  $N_\mu^{MC} = 127772$  was also compatible with the number in the beam  $N_b^{MC} = 127695$ , which also yielded a number of pions compatible with zero  $N_\pi = -77 \pm 505$ .

The Feldman-Cousins likelihood ratio ordering procedure [33] is a unified frequentist method to construct single- and double-sided confidence intervals for parameters of a given model adapted to the data. It provides a natural transition between single-sided confidence intervals, used to define upper or lower limits, and double-sided ones. It is particularly useful in the boundary of physical regions while providing a true confidence interval.

The Feldman-Cousins procedure was used to extract 90% confidence level bands for the pion contamination in the  $\pi \rightarrow \mu$  beam, as a function of the outcome of the statistical fit (Figure 12, left). Similarly, the Feldman-Cousins procedure was used to extract 90% confidence level bands for the pion contamination in the Monte Carlo (Figure 12, right). For a fitted pion contamination of  $N_\pi = -303 \pm 509$ , the Feldman-Cousins upper limit is found to be  $N_\pi < 902$  events, corresponding to a pion fraction of  $f_\pi < 0.69\%$  at 90% confidence level (C.L.). Similarly, based on a fitted value of  $N_\pi = -77 \pm 505$ , an upper level confidence limit for the number of pions from the Monte Carlo simulation is found to be  $N_\pi < 1101$  events, corresponding to a pion contamination fraction of  $f_\pi^{MC} < 0.86\%$  at 90% C.L. This is to be compared to the true pion contamination from the Monte Carlo simulation of  $0.22 \pm 0.01\%$ .

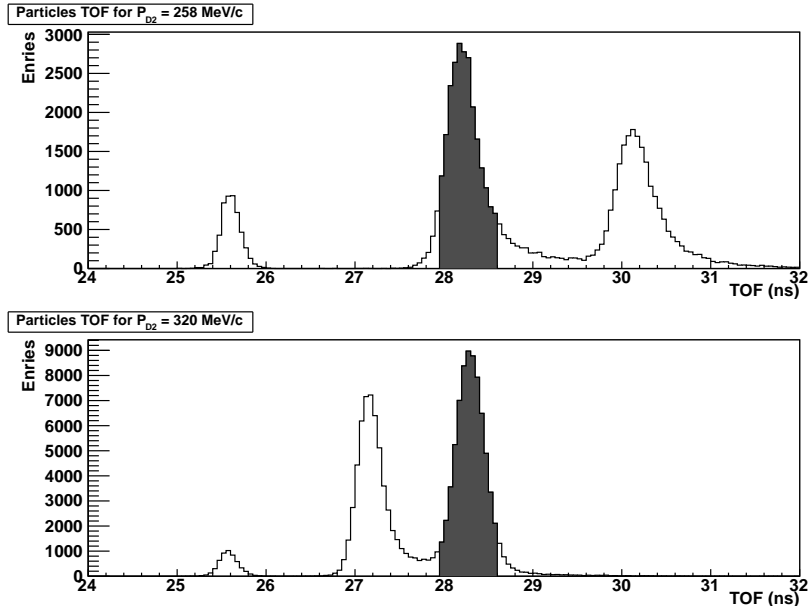


Figure 6: Time-of-flight distributions in two paired beam settings. The interval 28.0–28.6 ns (shaded) is populated by muons (pions) in the upper (lower) plot.

## 6 Systematic errors

The sources of systematic errors considered in this analysis were:

- Finer subdivision of the time-of-flight windows;
- Shift in the calibration of the time-of-flight windows;
- Binning of the KL ADC histograms;
- Effects of muon contamination in the pion templates (pion contamination in the muon template is found to be negligible).

The summary of systematic errors for both data and the Monte Carlo simulation on the pion contamination are found in Table 4. The systematic error due to the dependence on the time-of-flight distribution was determined by further subdividing the time-of-flight ranges associated to each point. Doubling the number of time-of-flight bins varies the fitted pion contamination by 0.18%. The dependence of the obtained pion fraction on the time-of-flight calibration is determined by shifting independently the time-of-flight values in the calibration runs by an amount compatible with the electron peak position ( $\pm 0.1$  ns). This results in a small variation in the pion contamination of 0.04% for data and 0.28% for Monte Carlo. The dependence on the histogram binning in the KL ADC distribution was also assessed by doubling and halving the bin-size to yield a variation in the fitted pion contamination of 0.18% in data and 0.16% in simulation. There is a bias in the determination of the pion contamination due to expected muon contamination in the pion template. For example, the nominal value is 25.1% muons in the pion template for point 1, 26.1% muons for point 2 and 26.2% muons for point 3. Setting the muon contamination in the pion template to zero in the Monte Carlo results in a shift in the pion contamination in the  $\pi \rightarrow \mu$  beam by 0.03%.

The quadratic sum of the total systematic errors is shown in the bottom row of Table 4. The total systematic error for the pion contamination is found to be 0.23% in data and 0.37% in Monte Carlo. These systematic errors are used to obtain the following yields:  $N_\pi = -303 \pm 509$  (stat) $\pm 299$  (syst) for the data and  $N_\pi = -77 \pm 505$  (stat) $\pm 472$  (syst) for the Monte Carlo. The statistical and systematic errors are added in quadrature and the Feldman-Cousins procedure is repeated to extract new upper limits of the number of pions in the  $\pi \rightarrow \mu$  beam

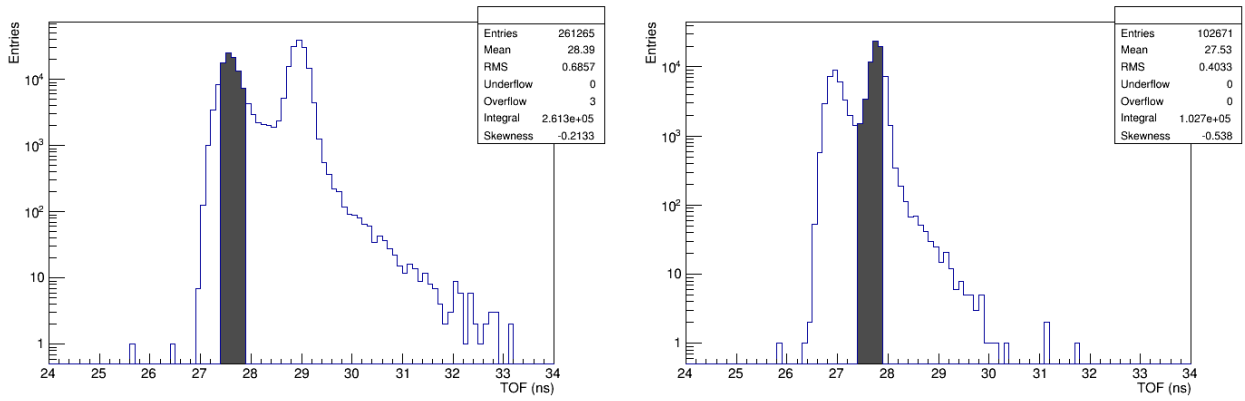


Figure 7: Monte Carlo simulation of the time-of-flight distributions of two paired beam settings. The interval 27.4–27.9 ns (shaded) is populated by muons (pions) in the left (right) plot.

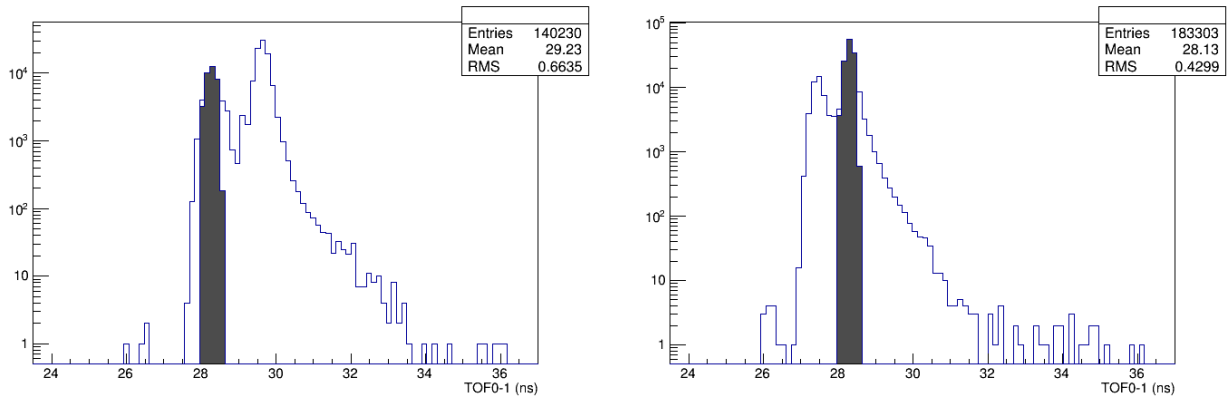


Figure 8: Monte Carlo simulation of the time-of-flight distributions of two paired beam settings. The interval 28.0–28.6 ns (shaded) is populated by muons (pions) in the left (right) plot.

of  $N_\pi < 1306$  events, corresponding to a contamination of  $f_\pi < 1.01\%$  at 90% C.L. including systematic errors. An upper level confidence limit for the Monte Carlo simulation with systematic errors was also derived to be  $N_\pi < 2131$  events, which corresponds to  $f_\pi^{MC} < 1.67\%$  at 90% C.L..

## 7 Conclusions

An upper level to the pion contamination in the MICE muon beam has been derived using precision time-of-flight counters in combination with the KL sampling calorimeter. The measurements were carried out in a variety of time-of-flight windows and the analysis yielded a pion contamination compatible with zero. The Monte Carlo expectation for a  $\pi \rightarrow \mu$  beam of  $6\pi$  mm·rad emittance and 200 MeV/c nominal momentum is  $(0.22 \pm 0.01)\%$ . The upper level for the pion contamination was found to be  $f_\pi < 0.69\%$  at 90% C.L., assuming statistical errors only and  $f_\pi < 1.0\%$  at 90% C.L., including statistical and systematic errors. A similar procedure applied to the Monte Carlo simulation yields a pion contamination of  $f_\pi < 0.86\%$  at 90% C.L., assuming statistical errors only and  $f_\pi < 1.7\%$  at 90% C.L., including statistical and systematic errors. Both data and simulation are compatible with each other and compatible with the expected fraction. This upper

## KL ADC Response

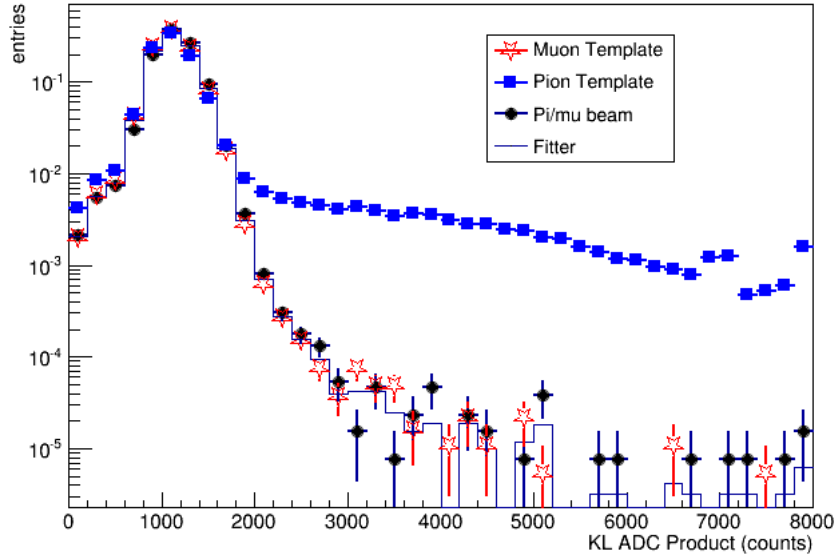


Figure 9: Muon template (red stars) and pion template (blue squares) for the sum of the three TOF data intervals from calibration runs, compared to MICE  $\pi \rightarrow \mu$  beam data (black dots). The line is the result of a fit of the  $\pi \rightarrow \mu$  beam to the fraction of pions and muons based on the two templates. Plots are normalised to unity.

Table 4: Sources of systematic errors in the evaluation of the pion contamination.

Effect	Assessment method	Absolute Impact on $\pi$ contamination	
		Data	MC
Time-of-flight distribution	finer subdivision	0.18%	0.18%
Time-of-flight calibration	shift calibrations by $\pm 0.1$ ns	0.04%	0.28%
Histogram binning	double/halve bin sizes	0.14%	0.16%
Bias due to contamination in templates	Create pure templates in MC	0.03%	0.03%
Total		0.23%	0.37%

level on the pion contamination of the MICE muon beam meets the experimental requirements to have a pion contamination below 1%, to be able to carry out a successful measurement of muon ionisation cooling.

## Acknowledgements

We gratefully acknowledge the help and support of the ISIS staff and of the numerous technical collaborators who have contributed to the design, construction, commissioning and operation of the experiment. In particular we would like to thank S. Banfi, F. Chignoli, R. Gheiger, A. Gizzi, V. Penna, R. Mazza and W. Spensley. We wish to acknowledge the essential contributions in the conceptual development of a muon cooling experiment made by P. Drumm, R. Edgecock, P. Fabricatore, R. Fernow, D. Findlay, W. Murray, J. Norem, P.R. Norton, K. Peach, C. Prior and N. McCubbin. We would also wish to acknowledge the work done in the early stages of the experiment by G. Barr, P. Chimenti, S. Farinon, G. Giannini, E. Radicioni, G. Santin, C. Vaccarezza, S. Terzo and K. Tilley. The experiment was made possible by grants from National Science Foundation and Department of Energy (USA), the Istituto Nazionale di Fisica Nucleare (Italy), the Science and Technology Fa-

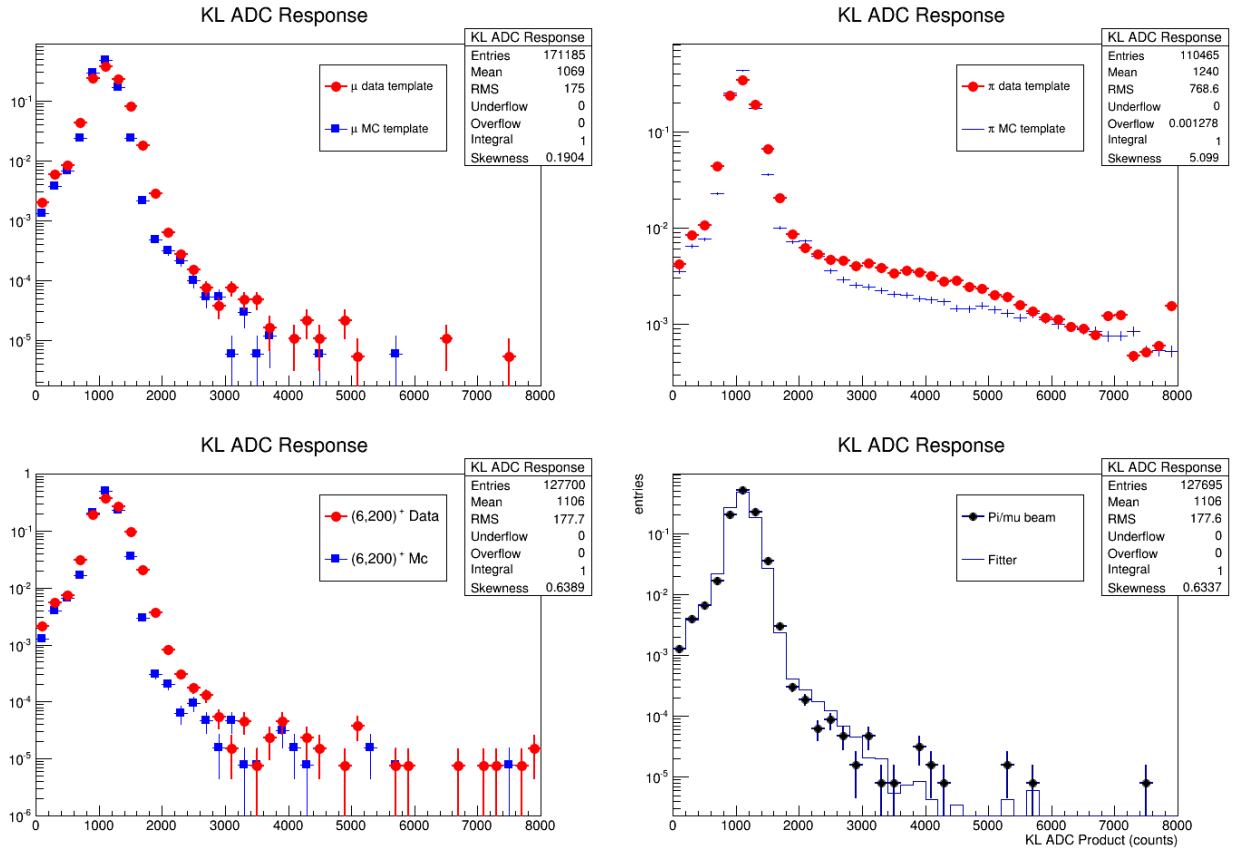


Figure 10: Monte Carlo simulation of the KL ADC product distributions for the muon template (top left), pion template (top right) and for the  $6\pi$  mm·rad, 200 MeV/c pion-muon beam (bottom left) for data and Monte Carlo. The bottom right plot shows the fit to the KL ADC product distribution of the Monte Carlo  $6\pi$  mm·rad, 200 MeV/c pion-muon beam.

300 cilities Council (UK), the European Community under the European Commission Framework Programe 7, the Japan Society for the Promotion of Science (Japan) and the Swiss National Science Foundation (Switzerland), in the framework of the SCOPES programme. We gratefully acknowledge their support. We also acknowledge the use of Grid computing resources deployed and operated by GridPP in the UK [34].

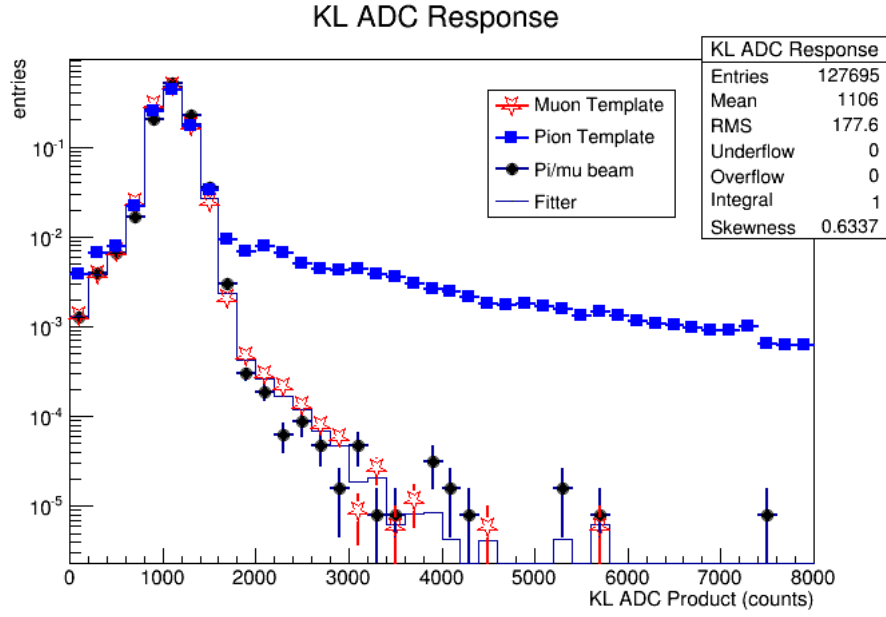


Figure 11: Monte Carlo simulation of the muon template (red stars) and pion template (blue squares) for the sum of the three TOF data intervals, compared to the simulated MICE  $\pi \rightarrow \mu$  beam data (black dots). The line is the result of a fit of the simulated  $\pi \rightarrow \mu$  beam to the fraction of pions and muons based on the two templates. Plots are normalised to unity.

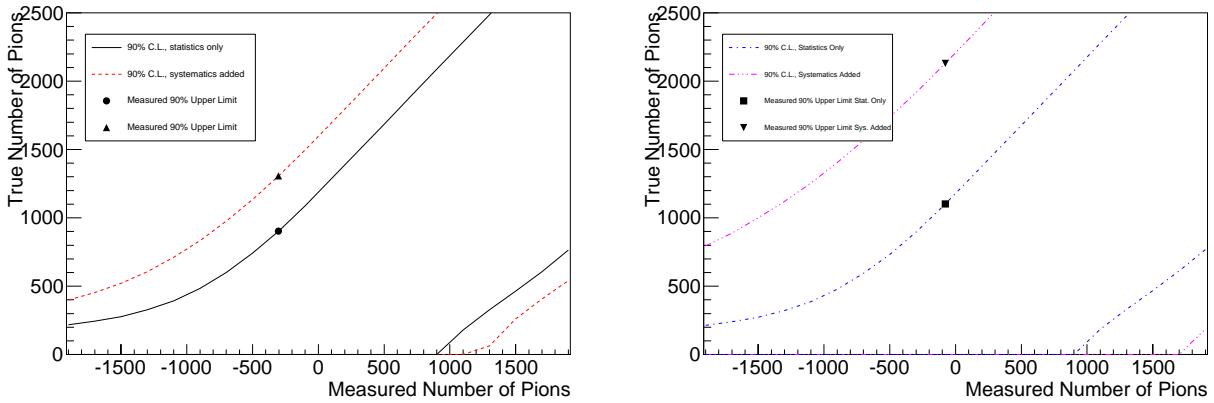


Figure 12: Feldman-Cousins statistical 90% confidence levels as a function of the results of the fitted number of pions for the comparison of the data with 129870 events (left) and Monte Carlo with 127772 events (right). The plots show the confidence level bands assuming the statistical error only and assuming a systematic error of 0.23% for the data and 0,37% for the Monte Carlo simulation that is added in quadrature to the statistical error.

## References

- [1] A. Blondel *et al.*, “Proposal to the Rutherford Appleton Laboratory: an international muon ionization cooling experiment (MICE),” *MICE-NOTE-21* (2003) .  
305 <http://hep04.phys.iit.edu/cooldemo/micenotes/public/pdf/MICE0021/MICE0021.pdf>.
- [2] D. G. Koshkarev, “Proposal for a decay ring to produce intense secondary particle beams at the SPS,” Tech. Rep. CERN/ISR-DI/74-62, CERN Internal Report, 1974.
- [3] S. Geer, “Neutrino beams from muon storage rings: Characteristics and physics potential,” *Phys.Rev.* **D57** (1998) 6989–6997, arXiv:hep-ph/9712290 [hep-ph].
- 310 [4] **Muon Collider/Neutrino Factory** Collaboration, M. M. Alsharo’a *et al.*, “Recent progress in neutrino factory and muon collider research within the Muon collaboration,” *Phys. Rev. ST Accel. Beams* **6** (2003) 081001, arXiv:hep-ex/0207031.
- [5] A. Blondel (Ed. ) *et al.*, “ECFA/CERN studies of a European neutrino factory complex,” *CERN-2004-002* (2004) .
- 315 [6] S. Choubey *et al.*, “International Design Study for the Neutrino Factory, Interim Design Report,” *IDS-NF-20* (2011), arXiv:hep-ex/1112.2853.
- [7] F. Tikhonin, “On the effects at colliding mu meson beams,” *JINR-P2-4120* (2008) , arXiv:hep-ph/0805.3961.
- 320 [8] S. Geer, “Muon colliders and neutrino factories,” *presented at 25th International Linear Accelerator Conference (LINAC10), Tsukuba, Japan, 12-17 Sep 2010* (2010) .
- [9] C. M. Ankenbrandt *et al.*, “Status of muon collider research and development and future plans,” *Phys.Rev.ST Accel.Beams* **2** (1999) 081001, arXiv:physics/9901022 [physics].
- [10] D. Neuffer, “Principles and applications of muon cooling,” *Part. Accel.* **14** (1983) 75.
- [11] S. Ozaki *et al.*, “Feasibility study 2 of a muon based neutrino source,” *BNL-52623*,  
325 <http://www.cap.bnl.gov/mumu/studyii/FS2-report.html> (2001) .
- [12] M. Ellis *et al.*, “The design, construction and performance of the MICE scintillating fibre trackers,” *Nucl. Instr. Meth* **A659** (2011) 136–159, arXiv:physics.ins-det/1005.3491 [physics.ins-det].
- [13] **MICE** Collaboration, D. Adams *et al.*, “Characterization of the muon beams for the Muon Ionization  
330 Cooling experiment,” *submitted to Eur. J. Phys. C* (2013) .
- [14] R. Bertoni *et al.*, “The design and commissioning of the MICE upstream time-of-flight system,” *Nucl.Instrum.Meth.* **A615** (2010) 14–26, arXiv:hep-ph/001.4426 [physics.ins-det].
- [15] M. Bonesini *et al.*, “Behaviour in magnetic fields of conventional and fine-mesh photomultipliers,” *Nucl.Instrum.Meth.* **A693** (2012) 130–137.
- 335 [16] L. Cremaldi, D. A. Sanders, P. Sonnek, D. J. Summers, and J. J. Reidy, “A Cherenkov Radiation Detector with High Density Aerogels,” *IEEE Trans.Nucl.Sci.* **56** (2009) 1475–1478, arXiv:hep-ph/0905.3411 [physics.ins-det].

- [17] R. Bertoni *et al.*, “Analysis of PID detectors (TOF and KL) performances in the MICE 2010 run,” *MICE-NOTE-DET-337* (2011). <http://hep04.phys.iit.edu/cooldemo/micenotes/public/pdf/MICE0337/MICE0337.pdf>.  
340
- [18] M. Bonesini *et al.*, “The Refurbishing of MICE TOF0 and TOF1 detectors,” *MICE-NOTE-DET-363* (2012). <http://hep04.phys.iit.edu/cooldemo/micenotes/public/pdf/MICE0363/MICE0363.pdf>.
- [19] D. Sanders, “MICE Particle Identification Systems,” *Particle Accelerator Conference (PAC09), Vancouver (2009)*, arXiv:hep-ph/0910.1332 [physics.ins-det].  
345
- [20] **MICE** Collaboration, M. Bogomilov *et al.*, “The MICE Muon Beam on ISIS and the beam-line instrumentation of the Muon Ionization Cooling Experiment,” *JINST* **7** (2012) P05009, arXiv:1203.4089 [physics.acc-ph].
- [21] M. Bonesini, “Progress of the MICE experiment at RAL,” *to be published on Nucl. Phys. B. Proc. Suppl.* (2013), arXiv:physics.acc-ph/1303.7363 [physics.acc-ph].  
350
- [22] R. Bertoni *et al.*, “The Construction of the MICE TOF2 detector,” *MICE-NOTE-DET-286* (2010). <http://hep04.phys.iit.edu/cooldemo/micenotes/public/pdf/MICE0286/MICE0286.pdf>.
- [23] F. Ambrosino *et al.*, “Calibration and performances of the KLOE calorimeter,” *Nucl.Instrum.Meth.* **A598** (2009) 239–243.  
355
- [24] C. Booth *et al.*, “The design, construction and performance of the MICE target,” *JINST* **8** (2013) P03006, arXiv:1211.6343.
- [25] S. Blot *et al.*, “Proton Contamination Studies in the MICE Beam Line,” *Proc. IPAC11* (2011).
- [26] T. Roberts, “G4beamline, A Swiss Army Knife for Geant4, optimized for simulating beamlines.”  
<http://g4beamline.muonsinc.com>.  
360
- [27] “MICE Analysis User Software (MAUS)”. <http://micewww.pp.rl.ac.uk/projects/maus/wiki>.
- [28] **KLOE** Collaboration, A. Di Domenico, “Kloe internal note 196.”
- [29] **HARP** Collaboration, U. Dore, “private communication.”
- [30] H. H. Tan, “A statistical model of the photomultiplier gain process with applications to optical pulse detection,” *The Telecommunications and Data Acquisition Progress Report* **42-68** (1982).  
[http://ipnpr.jpl.nasa.gov/progress\\_report/42-68/68H.PDF](http://ipnpr.jpl.nasa.gov/progress_report/42-68/68H.PDF).  
365
- [31] R. Brun and F. Rademakers, “ROOT - An Object Oriented Data Analysis Framework,” *Nucl. Instrum. Meth.* **389** (1997) 81–86.
- [32] R. Barlow and C. Beeston, “Fitting using finite Monte Carlo samples,” *Comp. Phys. Commun.* **77** (1993) 219–22.  
370
- [33] G. J. Feldman and R. D. Cousins, “A Unified approach to the classical statistical analysis of small signals,” *Phys.Rev.* **D57** (1998) 3873–3889, arXiv:physics/9711021 [physics.data-an].
- [34] D. Britton *et al.*, “GridPP: the UK grid for particle physics,” *Phil. Trans. R. Soc. A* **367** (2009) 2447–24.